

Micro-Electrode with Fast Mass Transport for Enhancing Selectivity of Carbonaceous Products in Electrochemical CO₂ Reduction

Qixing Zhang, Dan Ren, Sanjiang Pan, Manjing Wang, Jingshan Luo, Ying Zhao, Michael Grätzel, and Xiaodan Zhang*

During electrochemical carbon dioxide (CO₂) reduction on copper electrodes in an aqueous electrolyte, one of the key challenges is the competition between hydrogen evolution and CO₂ reduction, especially under large current density. Here, micro-electrodes are designed with a copper wire as the substrate, which shows improved mass transport compared to the planar electrode. The Faradaic efficiency for C₂₊ products reaches 79% with a partial geometric current density -77.7 mA cm^{-2} on Cu₂O nanowire/micro-electrode, which is 3.7 times higher than Cu₂O nanowire/planar-electrode. The authors also designed CuO and metallic Cu with micro-electrode as substrate and observed enhanced selectivity for carbonaceous products, proving the universality of the concept. The improved activity is attributed to the fast mass transport of CO₂ to the catalytic interface and thus the suppression of hydrogen production.

with appreciable amounts.^[11–13] However, achieving high selectivity of carbon-based products on Cu remains challenging and the competition with H₂ formation is ubiquitous in aqueous media.^[14] Besides, the partial current density for carbon-based products in H-cells still has a large gap with the practical target, which is at least 100 mA cm^{-2} .^[15–17] Many efforts have been devoted to improving the selectivity of Cu-based catalysts to hydrocarbons or oxygenates, such as morphology design,^[18–22] interface engineering,^[23–25] alloy, or doping,^[26–29] etc. However, achieving both high selectivity and large partial current density of multi-carbon products remains challenging, especially in H-cells.

1. Introduction

Converting carbon dioxide (CO₂) to fuels or chemicals using renewable energy is one of the promising ways to reduce our dependence on fossil fuels and mitigate the environmental impact of CO₂ emission.^[1–4] Electrochemical reduction of CO₂ powered by renewable electricity has attracted much attention since appreciable reaction rates have been achieved, and it promises a sustainable carbon-neutral economy.^[5–10]

Copper (Cu) is considered the only metal capable of catalyzing the reduction of CO₂ to hydrocarbons and oxygenates


This is believed to be caused by the low solubility and limited diffusion of CO₂ from the bulk electrolyte to the inner Helmholtz plane,^[30,31] leading to the competition of hydrogen production with CO₂ reduction, especially at higher current density.^[30] The mass transport rate can be estimated by:^[32–34]

$$M = \frac{D}{\delta_N} \quad (1)$$

Where D is the diffusion coefficient of CO₂, and δ_N is the Nernst diffusion layer thickness. The thinner diffusion layer will lead to faster mass transport based on Equation (1) and **Figure 1a**. Besides, compared to the planar-electrode with linear diffusion (**Figure 1b**), the diffusion pattern of cylindrical micro-electrode is nonlinear (**Figure 1c**), which will enhance the mass transport rate.^[33,34]

In this study, we synthesized Cu₂O nanowire onto a micro-sized Cu wire electrode with a radius of 50 μm, named Cu₂O-ME, to enhance the mass transport of CO₂. As a control sample, Cu₂O nanowire onto planar Cu mesh substrate, named Cu₂O-PE, was also used for CO₂ reduction. Cu₂O-ME exhibits enhanced selectivity of C₂₊ products and a remarkable partial current density, which are higher than those observed on Cu₂O-PE. In addition, CuO nanowire/micro-electrode (Hereafter referred to as a CuO-ME) and Cu/micro-electrode (Hereafter referred to as a Cu-ME) are also synthesized similarly. Interestingly, both micro-electrodes showed suppressed hydrogen evolution and enhanced CO₂ reduction process. The improved performance of all micro-electrodes is attributed to improved mass transport, leading to higher concentration of

Dr. Q. Zhang, S. Pan, M. Wang, Prof. J. Luo, Prof. Y. Zhao, Prof. X. Zhang
Institute of Photoelectronic Thin Film Devices and Technology
Key Laboratory of Photoelectronic Thin Film Devices and Technology of Tianjin
Ministry of Education Engineering Research Center of Thin Film Photoelectronic Technology
Renewable Energy Conversion and Storage Center
Solar Energy Conversion Center
Nankai University
Tianjin 300350, China
E-mail: xdzhang@nankai.edu.cn
Dr. D. Ren, Prof. M. Grätzel
Laboratory of Photonics and Interfaces
Institute of Chemical Sciences and Engineering
École Polytechnique Fédérale de Lausanne (EPFL)
Lausanne 1015, Switzerland

 The ORCID identification number(s) for the author(s) of this article can be found under <https://doi.org/10.1002/adfm.202103966>.

DOI: 10.1002/adfm.202103966

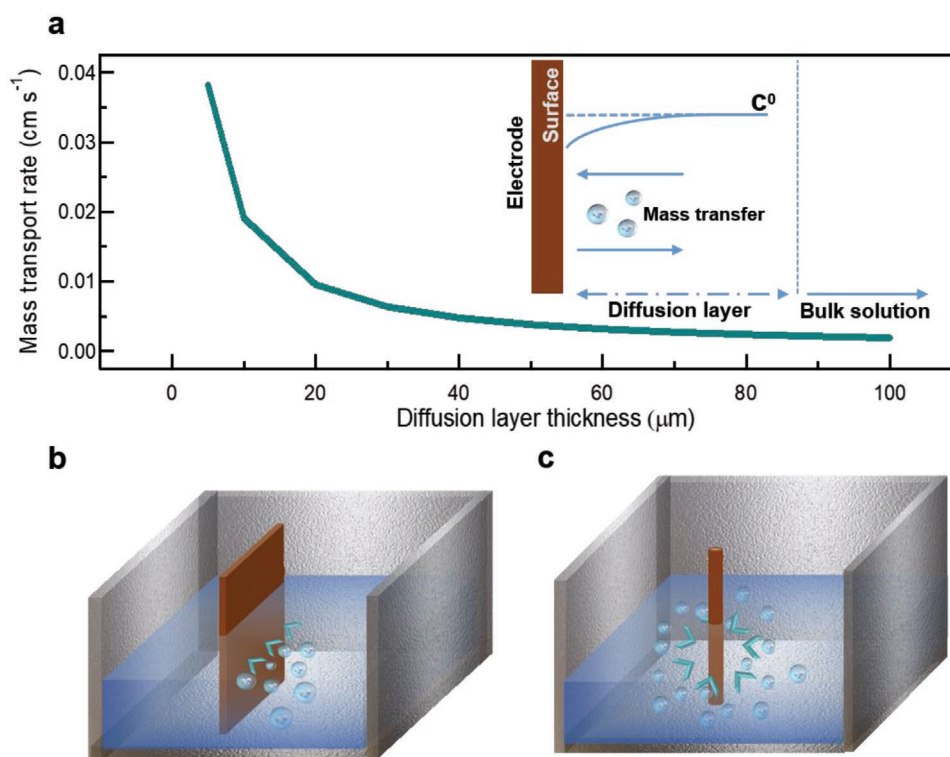


Figure 1. Schematic illustration of active substance diffusion on electrodes of different geometric shapes. a) The curve of the mass transport rate versus the diffusion layer thickness, the diffusion coefficient $D = 1.91 \times 10^{-5} \text{ cm}^2 \text{ s}^{-1}$.^[31] Insert images is the schematic diagram of the concentration of CO_2 on the surface of the electrode. The diffusion path of the active substance on b) planar-electrode and c) cylindrical micro-electrode (Radius = $50 \mu\text{m}$).

CO_2 on the surface of the electrode and the suppression of H_2 production. The conclusion achieved from the studied single micro-electrode with fast mass transport in electrocatalysis can be implemented to achieve more efficient commercially available electrodes in future and provides a new strategy to design electrodes for efficient CO_2 reduction.

2. Results

2.1. Synthesis and Characterization of Electrodes

Figure 2a illustrates the synthetic process for preparing Cu_2O nanowire electrodes (Cu_2O -NW). First, $\text{Cu}(\text{OH})_2$ NWs (Figure S1, Supporting Information) were obtained by anodic oxidation of Cu mesh at 10 mA cm^{-2} current density for 5 min in 3 M KOH and then transferred to a tube furnace for annealing at $500 \text{ }^\circ\text{C}$ for 3 h under argon environment to form Cu_2O planar electrode (Cu_2O -PE).^[35] Cu_2O micro-electrode (Cu_2O -ME) is consisted of only one mesh wire of Cu_2O -PE by simply removing one wire from the mesh.

The structure of Cu_2O -ME with micron size is illustrated in Figure 2b. They are composed of multiple grains with distinct grain boundaries. High-resolution TEM (HRTEM) image showed the lattice of Cu_2O (111) and Cu_2O (200) facets with lattice spacing values of 0.242 and 0.214 nm, respectively (Figure 2c). In addition, elemental Cu and O were uniformly distributed throughout the nanowire as identified by EDX mapping images (Figure 2d–f).

X-ray diffraction (XRD) patterns of Cu_2O -PE demonstrated the presence of Cu_2O and Cu (Figure 2g). The peaks at 36.9° and 42.6° could be assigned to Cu_2O (111) and Cu_2O (200), respectively, consistent with HRTEM. The peak at 43.3° could be assigned to Cu (111), originating from Cu mesh substrate. X-ray photoelectron spectroscopy (XPS) illustrated the features of $\text{Cu}^{(0/I)}$ at 932 and 952 eV (Figure 2h).^[36] The peaks at 934.4 and 954.5 eV indicated $\text{Cu}^{(II)}$ existing.^[37]

After the electrochemical prereluction process, the surface morphology of Cu_2O -ME and Cu_2O -PE still maintained a nanowire structure, and the grains on the nanowire showed no noticeable change (Figure S2a,b, Supporting Information). Besides the peaks at 38.8° and 42.6° assigned to CuO and Cu₂O respectively, the main peaks represent the Cu phase (Figure S2c, Supporting Information). Besides, the XPS result also verifies the $\text{Cu}^{(0/I)}$ and $\text{Cu}^{(II)}$ features (Figure S2d, Supporting Information).^[36,37] After CO_2 reduction testing, the surface morphology of Cu_2O -PE and Cu_2O -ME was characterized (Figure S3, Supporting Information). The nanowires become rough, which could be attributed to the reduction of Cu_2O to Cu during the electrocatalytic process.^[27]

2.2. Enhanced Selectivity of Cu_2O -ME for CO_2 Reduction to C_{2+} Products

The working electrode was electrochemically tested in an H-type reactor of a three-electrode setup (Figure S4, Supporting Information). Potentiostatic measurements from -0.7 to -1.15 V

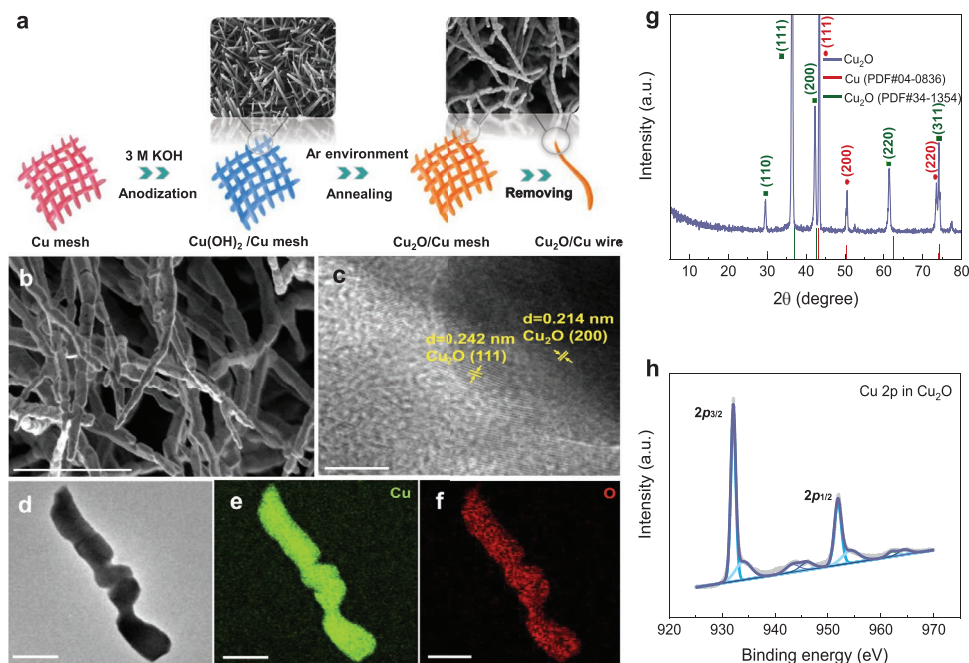


Figure 2. Preparation and chemical characterizations. a) Schematic diagram of preparation of Cu₂O-PE and Cu₂O-ME. b) SEM and c) HRTEM images of Cu₂O NWs. d) TEM, e) Cu, and f) O EDX mapping images of Cu₂O NWs. g) XRD patterns of Cu₂O NWs. h) High-resolution Cu 2p XPS spectra of Cu₂O NWs. Scale bars: 1 μ m and 5 nm for (b) and (c) respectively; 500 nm for (d–f).

versus RHE in CO₂-saturated 0.1 M KHCO₃ solution were carried out on Cu₂O-ME with 50 μ m and Cu₂O-PE with 100-mesh electrode. The current density remained stable during the 2000 s measurement (Figure S5, Supporting Information). Gas chromatography (GC) and high-performance liquid chromatography (HPLC) was used to analyze gas and liquid products, respectively.

The geometric current density j_{total} and partial geometric current density for CO₂ reduction ($j_{\text{CO}_2\text{RR}}$), C₂₊ products (j_{C_2+}), and H₂ (j_{H_2}) were calculated on each electrode in the potential range from -0.7 to -1.15 V (Figure 3a,b). j_{total} and $j_{\text{CO}_2\text{RR}}$ on Cu₂O were improved compared to the value on Cu₂O-PE (Figure 3a). The Cu₂O-ME also achieved an impressive j_{C_2+} of -77.7 mA cm⁻² (Figure 3b), while j_{C_2+} only reached -20.8 mA cm⁻² for the Cu₂O-PE at -1.15 V.

The FE values for hydrogen (H₂), ethylene (C₂H₄), ethanol (C₂H₅OH), and other C₂₊ products on the Cu₂O-ME and Cu₂O-PE at different applied potentials are shown in Figure 3c,d. By comparing the product distributions at optimal potentials, we found that the total C₂₊ FE on Cu₂O-ME added up to 79% at -1.15 V, while the FE of 49% was achieved on Cu₂O-PE. An ethylene FE of 42% and ethanol FE of 34% on Cu₂O-ME was achieved with a current density of -41.6 mA cm⁻² and -34.0 mA cm⁻² at -1.15 V, respectively (Figure 3c, Tables S1–S4, Supporting Information). A distinctively different selectivity of H₂ was observed on Cu₂O-ME and Cu₂O-PE (Figure 3d). The C₂₊ products-to-hydrogen ratio increased from 1.13 on Cu₂O-PE to 4.34 on Cu₂O-ME at -1.15 V. This result indicates that increasing the mass transport of CO₂ helps suppress hydrogen evolution effectively.

The diameter of ME was also studied by using Cu₂O-ME from different mesh substrates. Comparing the Cu₂O-ME with

50 μ m size, the FE of the C₂₊ on the larger micro-electrode with 90 μ m decreased at -1.05 V, and the FE of C₂₊ on the Cu₂O-ME with 25 μ m was also slightly reduced at -1.1 V (Figure S6 and Tables S5,S6, Supporting Information). The above results illustrated that the size of micro-electrode influences the selectivity of C₂₊ under different applied potential. Still, all of the micro-electrode successfully suppressed hydrogen generation and promoted the selectivity of multi-carbon products. The performance of the Cu₂O-PE with different mesh numbers was also studied. Similar selectivity of C₂₊ products was achieved on Cu₂O-PE with 60 mesh, 100 mesh, and 150 mesh at -1.05 V (Figure S7 and Tables S7,S8, Supporting Information), but the Cu₂O-PE with 100 mesh has the best selectivity for multi-carbon products at -1.15 V. Faradaic efficiency of C₂₊ products at the optimal current density was summarized in Figure S8, Supporting Information, showing our Cu₂O-ME with a diameter of 50 μ m shows the highest current density for multi-carbon products.

The stability of the Cu₂O-ME was evaluated at -1.15 V in 0.1 M KHCO₃ electrolyte for 10 h. The performance was maintained during long-term electrolysis, and the average FE of 70% for C₂₊ products was achieved (Figure S9, Supporting Information). After the stability test, the surface morphology of Cu₂O-ME becomes rough (Figure S10, Supporting Information) due to the reduction of Cu₂O to Cu during the CO₂ reduction reaction. XPS results demonstrated that peaks at 932.2 eV and 952.1 eV were attributed to Cu^{(0)/(I)} (Figure S10b, Supporting Information). The small peaks at 934.8 and 954.7 eV assigned to Cu^(II) were attributed to quick oxidation when exposed to air. HRTEM further verified that Cu₂O was reduced to Cu after a long-term reaction (Figure S10d, Supporting Information).

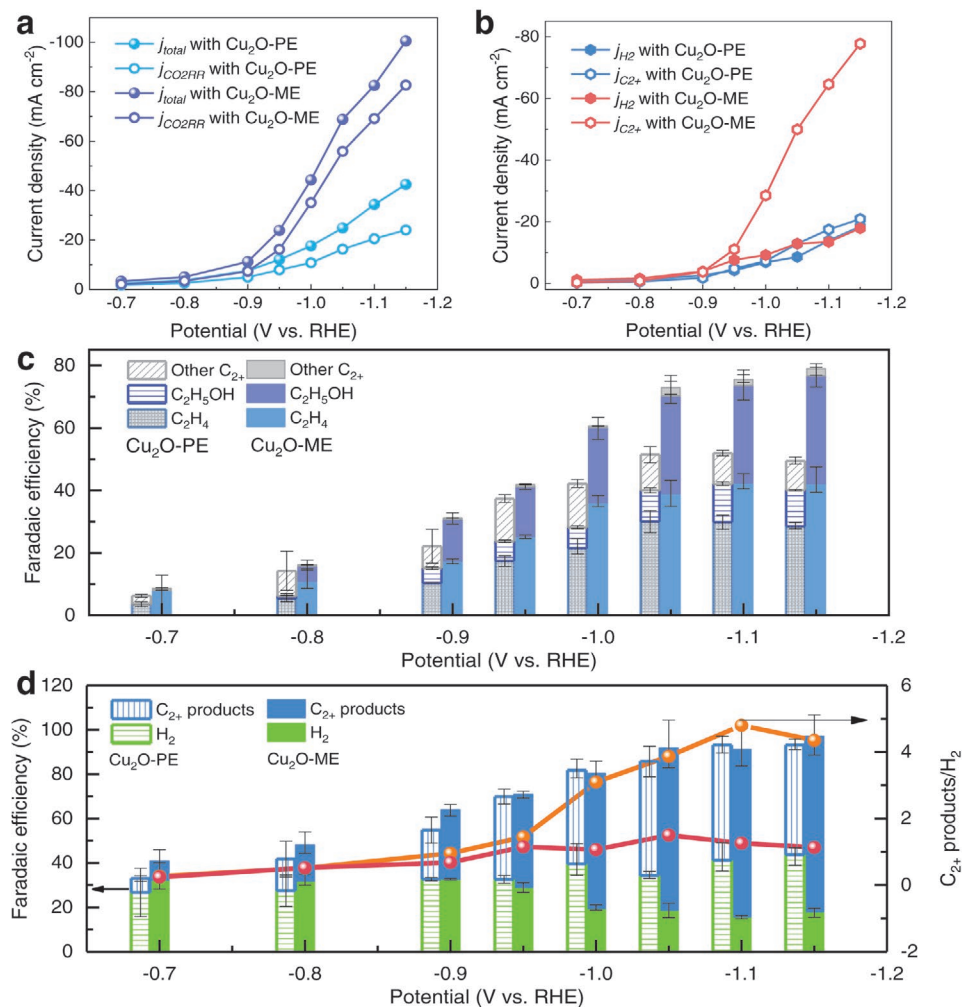


Figure 3. CO₂ performance comparisons on Cu₂O-ME and Cu₂O-PE. a) Total current density (j_{total}) and partial current density of CO₂ reduction ($j_{\text{CO}_2\text{RR}}$). b) The partial current density of H₂ (j_{H_2}) and C₂₊ products (j_{C_2+}). c) Faradaic efficiency of ethylene, ethanol, and other C₂₊ products. d) Faradaic efficiency of all C₂₊ products and hydrogen, and the Faradaic efficiency ratio of C₂₊ products to hydrogen. Orange stands for Cu₂O-ME and red for Cu₂O-PE.

2.3. Effect of the Electrochemical Active Surface Area on the Rate of Formation for C₂₊ Products

To evaluate the intrinsic catalytic activity, the electrochemically active surface area (ECSA) of both electrodes was calculated (Figure S11 and Table S17, Supporting Information). The specific current densities are shown in Figure 4a,b. Cu₂O-ME still has a more significant specific current density than Cu₂O-PE at the applied potential (Figure 4a,b), demonstrating enhanced activity of the micro-electrode. The smaller specific current density of hydrogen was observed on Cu₂O-ME, which indicated that hydrogen evolution was suppressed at potential <−1.05 V. These results demonstrated that the micro-electrode with fast mass transport increased the concentration of CO₂ on the surface, contributing to enhanced selectivity of multi-carbons products was achieved by suppressing the hydrogen.

To understand the effect of the micro-electrode on enhanced C₂₊ products, we further quantitatively analyzed the production

rate of *CO (TOF_{CO}), which is composed of gas (TOF_{CO(g)}) and be further reduced CO (TOF_{*CO}) (Figure 4c). TOF_{*CO} is enhanced from 410.3 nmol s^{−1} cm^{−2} on Cu₂O-PE to 1431.2 nmol s^{−1} cm^{−2} on Cu₂O-ME at −1.15 V, where $\Delta\text{TOF}_{*CO} = 1020.9 \text{ nmol s}^{-1} \text{ cm}^{-2}$. The production rate of CO gas increased from 29.2 nmol s^{−1} cm^{−2} on Cu-PE to 38.4 nmol s^{−1} cm^{−2} on Cu₂O-ME, where $\Delta\text{TOF}_{\text{CO(g)}} = 9.2 \text{ nmol s}^{-1} \text{ cm}^{-2}$. That is to say, only 9.2 nmol s^{−1} cm^{−2} of the increased CO was released to form CO gas, while 99% of CO was further reduced to C₂₊ products, which proved that a higher ratio of CO intermediate was reduced to multi-carbon products on Cu₂O-ME.

Operando Raman spectroscopy was used to identify key reaction intermediates on Cu₂O-ME (Figure S12, Supporting Information) in CO₂-saturated 0.1 M KHCO₃. Three bands at 275–285, 354–362, and 2070–2080 cm^{−1} were recorded. They can be attributed to the adsorbed CO intermediates on the surface.^[27,29,38] The bands at 2844 and 2912 cm^{−1} could be assigned to C–H containing intermediates.^[27,39] Above results illustrate that these intermediates were vital to the formation of

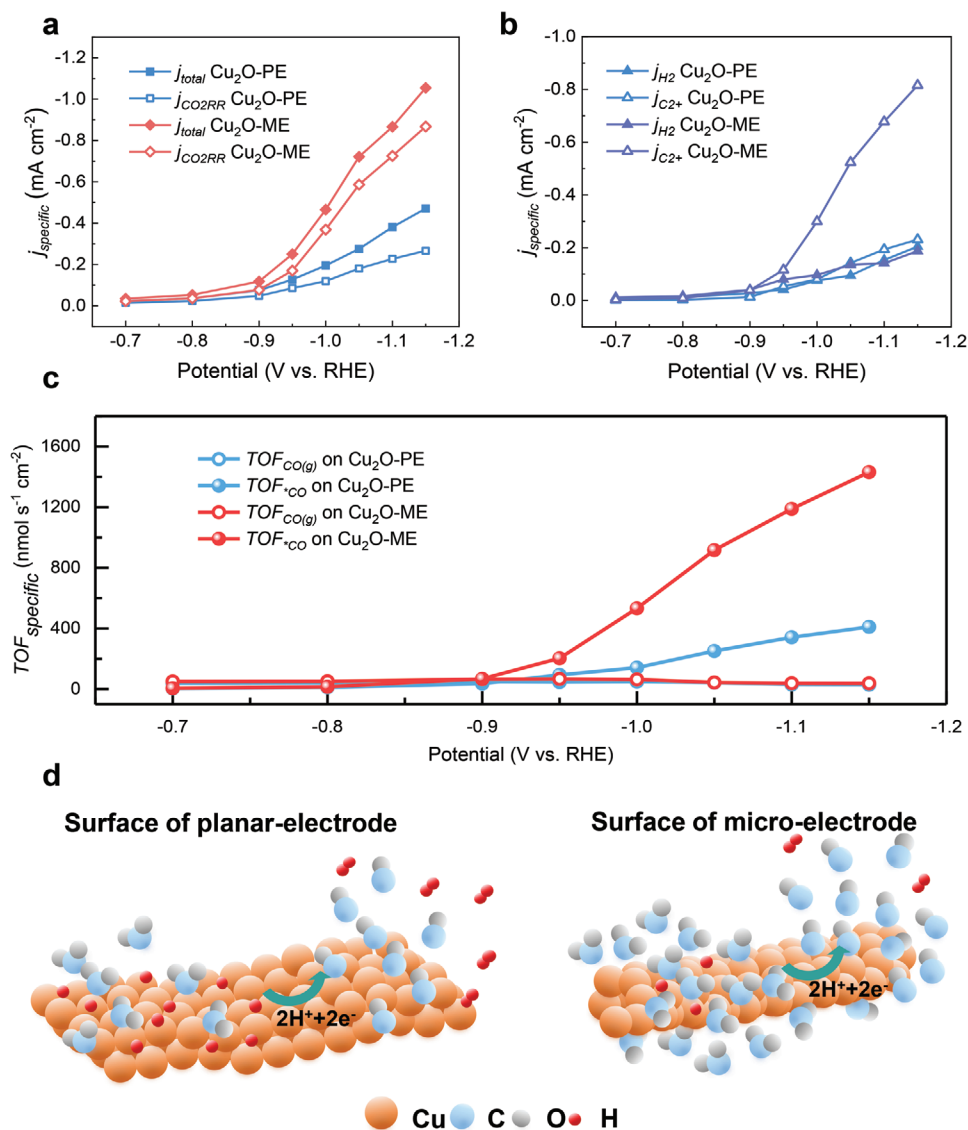


Figure 4. The intrinsic activity of Cu₂O-ME and Cu₂O-PE. a) Values for the total current density (j_{total}) and CO₂ reduction partial current density (j_{CO2RR}) on Cu₂O-PE and Cu₂O-ME within the potential range -0.7 to -1.15 V, respectively. b) hydrogen partial current density (j_{H_2}) and C₂₊ partial current density (j_{C_2+}) on Cu₂O-PE and Cu₂O-ME within the potential range -0.7 to -1.15 V, respectively. c) Quantitative analysis of the turnover frequency for producing (TOF_{CO})_{gas} (TOF_{CO(g)}) and for forming reduced CO (TOF_{*CO}) on Cu₂O-PE and Cu₂O-ME within the potential range -0.7 to -1.15 V, respectively. d) Schematic illustration of the suppression of hydrogen formation and improved concentration of CO intermediate at Cu₂O-PE and Cu₂O-ME.

hydrocarbons or oxygenates. In addition, bands at 503–586 and 703–752 cm⁻¹ were proposed to be assigned to adsorbed OH group and in-plane bending $\delta(\text{CO}_2^-)$ vibrations of (C, O)-CO₂⁻, respectively.^[40] The formed OH group is due to the existed nucleation site for hydroxylation on the subsurface oxygen of Cu₂O-ME in an aqueous solution. The band at 1054 cm⁻¹ was considered to adsorbed CO₃²⁻, which formed by bicarbonate reacts with hydroxide during CO₂ reduction reaction.^[40–42]

Electrochemical impedance spectroscopy can be used to measure the thickness of the diffusion layer (Figure S13, Supporting Information).^[43] The diffusion layer thickness δ was estimated to be 123 and 40.3 μm on Cu₂O-PE and Cu₂O-ME electrodes, respectively. As shown in Figure 1a, the mass

transfer rate is inversely proportional to the thickness of the diffusion layer. Therefore, the above results quantitatively confirmed that the micro-electrode with fast mass transport decreased the thickness of the diffusion layer, contributing to increased concentration of CO₂ on the surface of the electrode.

The schematic concentration of CO₂ near the surface was illustrated in Figure 4d, illustrating more CO₂ near the surface of micro-electrode. A higher concentration of CO intermediate formed covers the micro-electrode surface which attributing to the fast mass transport, increased the concentration of CO₂, leading to enhanced further reduced CO to multi-carbon products and inhibited the formation of hydrogen.

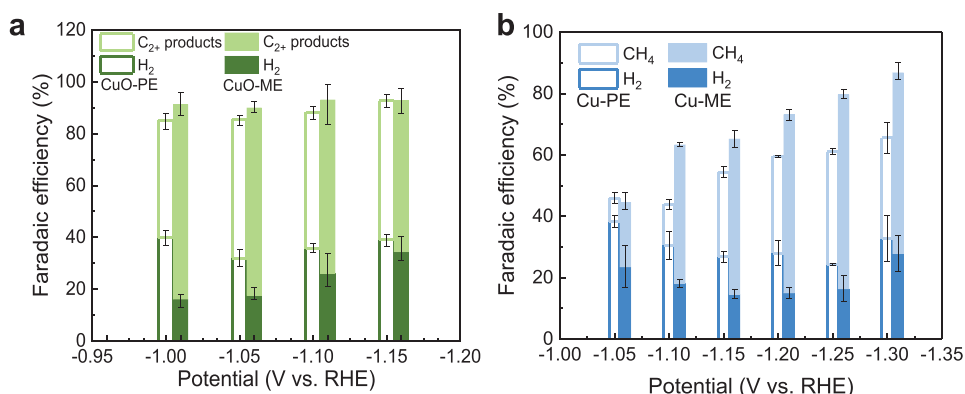


Figure 5. CO₂ performance on CuO-ME and Cu-ME. a) Faradaic efficiency of all C₂₊ products and H₂ of CuO-PE and CuO-ME. b) Faradaic efficiency of CH₄ and H₂ of Cu-PE and Cu-ME.

2.4. Universality of the Concept

CuO-ME and Cu-ME were prepared to verify that different materials with different structures also fit into this design strategy. The CuO NWs exhibited ribbed structure (Figure S14, Supporting Information) and Cu-ME shows a plane surface with some folds (Figure S15, Supporting Information). Comparing with the planar electrode, similar results were achieved, where the FE of H₂ was suppressed on both CuO-ME and Cu-ME (Figure 5, Tables S9–S12, Supporting Information). Formation of C₂₊ products and CH₄ were maximized on the CuO-ME and Cu-ME with FE of 75% at –1.0 V and 63% –1.25 V, respectively. The CuO-PE and Cu-PE with different mesh numbers were also prepared. As increased the mesh number, the FE of H₂ increased. And the CuO-PE and Cu-PE with different mesh numbers shown similar selectivity of CO₂ reduction to multi-carbons and CH₄ products, respectively (Figure S16 and Tables S13–S16, Supporting Information). To demonstrate the intrinsic activity of each electrode, the ECSA was also estimated (Figures S17,S18 and Tables S18,S19, Supporting Information). The conversion efficiency of CO being further reduced based on specific TOF_{CO} was calculated to be ~100% on CuO-ME at –1.0 V and ~96% on Cu-ME at –1.20 V, respectively (Figures S19 and S20, Supporting Information).

This work is different from previously published works using nanowire substrates,^[44–45] where researchers employed substrates with multiple nanowires. These electrodes experience serious mass transport issues, especially at large overpotentials. In contrast, this work uses a single nanowire which has improved mass transport. The current density and faradaic efficiency of C₂₊ products have been improved significantly.

3. Conclusions

In summary, we designed the Cu₂O-ME for CO₂ reduction and achieved Faradaic efficiency of 79% to C₂₊ products with a partial current density of –77.7 mA cm^{–2}. The Faradaic efficiencies of the products demonstrate that this micro-electrode can effectively suppress hydrogen production, yielding enhanced C₂₊ products. The results of the production rate of CO further illustrate that the chance of the contact between CO intermediates

and the surface of Cu₂O-ME is increased, favoring C–C coupling to C₂₊ products. CuO-ME and Cu-ME were also prepared, and the improved performance further verified the universality of this strategy. In general, faster mass transport on micro-electrode leads to a thinner diffusion layer that does not expand with time, contributing to a higher concentration of CO on the surface of the electrode and improving the selectivity of hydrocarbons or oxygenates. This work will provide a novel idea and general way for catalyst design.

4. Experimental Section

Chemicals: All reagents were used without further purification unless noted. All solutions were prepared with 18.2 MΩ·cm deionized water. Potassium bicarbonate (KHCO₃, ≥99.95%, Sigma-Aldrich), potassium hydroxide (KOH, 99.999%, Sigma-Aldrich), Hydrochloric acid (HCl, analysis pure). Cu mesh (99.99%, 60, 100, and 150 mesh) was purchased from Hebei Zhanmo metal materials.

Cu₂O-PE and Cu₂O-ME: Cu mesh was cleaned with ethanol and HCl to remove the surface organics and oxides. Then Cu mesh was oxidized in 3 M KOH at 10 mA cm^{–2} current density to form Cu(OH)₂ nanowires/Cu mesh. Deionized water was used to remove residual KOH. Cu(OH)₂ nanowires/Cu mesh was transferred to a tube furnace under an Ar environment for heat treatment. The furnace was programmed to heat at a rate of 5 °C per min to 500 °C and was maintained at 500 °C for 3 h. The furnace was cooled down to room temperature to form Cu₂O nanowire/Cu mesh (Cu₂O-PE). Cu₂O micro-electrode was prepared by taking one wire from Cu₂O nanowire/Cu mesh (Cu₂O-ME).

CuO-PE and CuO-ME: Cu(OH)₂ nanowires/Cu mesh was synthesized by a similar process as Cu₂O-PE except for the heat treatment step. Cu(OH)₂ nanowires/Cu mesh were annealed in a muffle furnace under an air environment at 200 °C for 2 h.

Cu-PE and Cu-ME: Cu mesh as the Cu-PE after cleaned by ethanol and HCl in turn. Cu micro-electrode was prepared by taking one wire from the Cu mesh, as Cu-ME.

Material Characterization: SEM images were taken using an Apreo S LoVac microscope. Structural characterization of electrodes was obtained using XRD (Rigaku) with Cu K_α radiation. XPS data were acquired by Thermo Scientific ESCALAB 250Xi with an Al K_α source. TEM characterizations were performed using a JEM-2800 with a field emission gun operated at 200 kV.

Operando Raman spectroscopy: Horiba XPlORA confocal Raman microscope, equipped with a diode laser of 638 nm with 30 mW power, was used for operando Raman spectroscopy. A water immersion objective (100×, Olympus) was used for all the measurements. A Teflon FEP parafilm (Dupon, 25 μm thickness) was used to cover the objective

with a water drop between parafilm and objective. 0.1 M KHCO₃ was used as the electrolyte, and CO₂ continuously flowed into the electrolyte during measurement. Ag/AgCl (saturated KCl) and electrodeposited IrO₂ were used as the reference and counter electrode, respectively. Spectra were presented as they were without any background smoothing or subtraction.

Electrocatalytic Measurements: Electrochemical tests were performed using an Autolab Pgstat204 potentiostat in an H-cell. The H-cell includes two compartments, separated by an anion exchange membrane under ambient conditions. The measurements were carried out in a three-electrode system. Ag/AgCl, as the reference electrode, was placed in the cathodic compartment. IrO₂/Ti foil was used as a counter electrode. CO₂-saturated 0.1 M KHCO₃ solution was used as the electrolyte, which was stirred at a rate of 1500 rpm during electrolysis. Besides, CO₂ gas flow was controlled by a mass flow controller at a specified flow rate of 10 sccm. The applied potentials were IR-compensated and were converted to the RHE scale.

During electrolysis, gas-phase products from the H-cell were quantified by a GC (Thermo scientific, Trace 1310) equipped with N₂ as the carrier gas. Liquid products were analyzed using HPLC (Agilent 1260 Infinity II) with 0.5 mM H₂SO₄ as the mobile phase. Typically, 900 μL of the post-electrolysis catholyte was mixed with 100 μL of 4.5 M H₂SO₄ to neutralize the electrolyte before sampling.

ECSA Measurement: ECSAs of the electrodes were quantified by measuring double layer capacitances. Cyclic voltammetry measurements were carried out at a potential window with no faradaic process at scan rates of 20, 40, 60, 80, and 100 mV s⁻¹ (Figures S7, S11, and S12, Supporting Information). The curve of the non-faradaic current densities versus the scan rate was plotted, and the slope of this curve was calculated. The rough factors were obtained by the following equation: RF = C_{DL}/C_S, where specific capacitance C_S = 0.03 mF cm⁻².^[46]

Calculation of the Turnover Efficiency (TOF): The production rate of CO intermediate (TOF_{CO}) consisted of CO gas (TOF_{CO(g)}) and CO (TOF_{*CO}) that was being further reduced:

$$\text{TOF}_{\text{CO}} = \text{TOF}_{\text{CO(g)}} + \text{TOF}_{*\text{CO}} \quad (2)$$

Where TOF_{*CO} was calculated as:

$$\begin{aligned} \text{TOF}_{*\text{CO}} = & \text{TOF}_{\text{CH}_4} + 2\text{TOF}_{\text{C}_2\text{H}_4} + 2\text{TOF}_{\text{C}_2\text{H}_6} + 2\text{TOF}_{\text{CH}_3\text{COOH}} \\ & + 2\text{TOF}_{\text{C}_2\text{H}_5\text{OH}} + 3\text{TOF}_{\text{C}_3\text{H}_6\text{O}} + 3\text{TOF}_{\text{C}_3\text{H}_8\text{O}} + 3\text{TOF}_{\text{C}_3\text{H}_7\text{OH}} \end{aligned} \quad (3)$$

In the case of the CO products, the equation of TOF_{CO} was calculated by:

$$\text{TOF}_{\text{CO}} = \frac{j_{\text{specific}}}{nF} \quad (4)$$

Where F is the Faradaic constant, n is the transfer electron number and j_{specific} is the specific partial current density.

The conversion efficiency of further reduced CO was estimated by:

$$\text{Efficiency} = \frac{\Delta\text{TOF}_{*\text{CO}}}{\Delta\text{TOF}_{*\text{CO}} + \Delta\text{TOF}_{\text{CO(g)}}} \times 100\% \quad (5)$$

The difference of TOF_{CO} between Cu₂O-PE and Cu₂O-ME was calculated as the amount of CO produced on active sites, defined here as ΔTOF_{CO}.

Calculation of the Faradaic efficiency of CO₂ Reduction: The Faradaic efficiency of the product f was calculated by the equation:

$$\text{FE}(f) = \frac{\text{Number of electrons required to produce } f}{\text{Total number of electrons for CO}_2 \text{ reduction}} \times 100\% \quad (6)$$

The partial current density of the product f was calculated by the equation:

$$j_f = j_{\text{total}} \times \text{FE}(f) \quad (7)$$

Faradaic efficiency of gas products f :

$$N_{\text{total}} = \frac{I_0 \times t}{e} = \frac{I_0 \times t}{1.602 \times 10^{-19} \text{C} / e} \quad (8)$$

Where I_0 is the average current obtained from the chronoamperogram. The time t is taken to fill the sample loop is: $t = \frac{V_0}{\nu}$. V_0 is the volume of the sample loop for hydrocarbons in the GC. ν is the flow rate of the CO₂ gas. The final equation of N_{total} is:

$$N_{\text{total}} = \frac{I_0 \times V_0}{e \times \nu} = \frac{I_0 \times V_0}{\nu \times 1.602 \times 10^{-19} \text{C} / e} \quad (9)$$

The equation of the number of electrons required to produce f (N_f) is:

$$N_f = x_0 \times n \times N_A \times m_f e \quad (10)$$

Where x_0 is the achieved ppm of the f . m_f is the number of electrons required to form 1 molecule of f .

According to the ideal gas law, n is the amount of gas in each sample loop V_0 under ambient temperature:

$$n = \frac{P \times V_0}{R \times T} \quad (11)$$

The final equation of N_f is:

$$N_f = \frac{x_0 \times N_A \times m_f e \times P \times V_0}{R \times T} \quad (12)$$

The equation of the Faradaic efficiency of the product f is:

$$\text{FE}(f) = \frac{N_f}{N_{\text{total}}} = \frac{x_0 \times N_A \times m \times P \times \nu \times 1.602 \times 10^{-19}}{I_0 \times R \times T} \times 100\% \quad (13)$$

Faradaic Efficiency of Liquid Products L :

$$\text{FE}(L) = \frac{N_L}{N_{\text{total}}} \quad (14)$$

The equation of N_{total} is:

$$N_{\text{total}} = \frac{Q_0}{e} = \frac{Q_0}{1.602 \times 10^{-19} \text{C} / e} \quad (15)$$

Where Q_0 is the total charge during the CO₂ reduction process.

The equation of N_L is:

$$N_L = C_L \times V \times N_A \times m_2 e \quad (16)$$

Where V is the volume of catholyte. m_2 is the number of electrons required from 1 molecule of L . C_L is the concentration of L in the catholyte.

The equation of the Faradaic efficiency of the product L is:

$$FE(L) = \frac{C_L \times V \times N_A \times m_2 \times 1.602 \times 10^{-19}}{Q_0} \times 100\% \quad (17)$$

Details of Faradaic Efficiency Calculation: In order to verify the accuracy of the FE calculation formula, the CO₂ reduction results of Cu₂O-ME at -1.15 V were used as an example to calculate the value of FE (Table S20, Supporting Information).

Faradaic efficiency of C₂H₄ gas product: V₀ is the volume of the sample loop in GC is 1 cm³, the flow rate of CO₂ is $\nu = 10 \text{ cm}^3 \text{ min}^{-1}$. Therefore, to fill the sample loop, the time t is:

$$t = \frac{V_0}{\nu} = \frac{1 \text{ cm}^3}{10 \text{ min}^{-1}} = 0.1 \text{ min} = 6 \text{ s} \quad (18)$$

n is the amount of gas in each sample loop V₀ under ambient temperature:

$$n = \frac{P \times V_0}{R \times T} = \frac{1.013 \times 10^5 \text{ Pa} \times 1 \times 10^{-6} \text{ m}^3}{8.314 \text{ J} \cdot \text{K}^{-1} \cdot \text{mol}^{-1} \times 299.150 \text{ K}} = 4.073 \times 10^{-5} \text{ mol} \quad (19)$$

C₂H₄ of vial 4 as an example. The number of electrons required to form 1 molecule of C₂H₄ is 12. The number of electrons ($N_{C_2H_4}$) needed to get x_0 ppm of ethylene is:

$$N_f = x_0 \times n \times N_A \times m_1 e = 156.66 \times 10^{-6} \times 4.073 \times 10^{-5} \text{ mol} \times 6.02 \times 10^{23} \text{ mol}^{-1} \times 12e = 4.6094 \times 10^{16} e \quad (20)$$

According to the injection time to fill up vial 4, the recorded current is $I_0 = 2.9999 \text{ mA}$ (this data was obtained from the chronoamperogram). Total number of electrons (N_{total}) measured during this sampling period:

$$N_{\text{total}} = \frac{I_0 \times t}{e} = \frac{2.9999 \times 10^{-3} \times 6 \text{ s}}{1.602 \times 10^{-19} \text{ C/e}} = 1.1236 \times 10^{17} e \quad (21)$$

Hence,

$$FE(C_2H_4) = \frac{N_{C_2H_4}}{N_{\text{total}}} \times 100\% = \frac{4.6094 \times 10^{16} e}{1.1236 \times 10^{17} e} \times 100\% = 41.02\% \quad (22)$$

Faradaic Efficiency of C₂H₅OH Liquid Product: C₂H₅OH as an example for calculation. 12 electrons were required to form one ethanol molecule from two CO₂ molecules. The volume of catholyte is $V = 10 \text{ cm}^3$. The equation of the produced ethanol $N_{C_2H_5OH}$ is:

$$N_{C_2H_5OH} = C_{C_2H_5OH} \times V \times N_A \times 12e = 0.191 \times 10^{-3} \text{ mol L}^{-1} \times 10 \times 10^{-3} \text{ L} \times 6.02 \times 10^{23} \text{ mol}^{-1} \times 12e = 1.38 \times 10^{19} e \quad (23)$$

From the chronoamperogram, the total charge is 6.24 C (Q_0). Hence, the equation of the N_{total} is:

$$N_{\text{total}} = \frac{Q_0}{e} = \frac{6.24 \text{ C}}{1.602 \times 10^{-19} \text{ C/e}} = 3.895 \times 10^{19} e \quad (24)$$

The faradaic efficiency of C₂H₅OH is:

$$FE(C_2H_5OH) = \frac{N_{C_2H_5OH}}{N_{\text{total}}} \times 100\% = \frac{1.38 \times 10^{19} e}{3.895 \times 10^{19} e} \times 100\% = 35.4\% \quad (25)$$

Calculations were repeated for all other products.

Supporting Information

Supporting Information is available from the Wiley Online Library or from the author.

Acknowledgements

This work was supported by the following projects: International Cooperation Projects of the Ministry of Science and Technology (2014DFE60170), the Strategic Japanese–Swiss Science and Technology Program from the Swiss National Science Foundation (project No. IZJSZ2_180176), the Sino-Swiss Science and Technology Cooperation (SSSTC) 2016 project from the Swiss National Science Foundation (project No. IZLCZ2_170294), the National Natural Science Foundation of China (Grant No. 61674084), the Overseas Expertise Introduction Project for Discipline Innovation of Higher Education of China (Grant No. B16027), Tianjin Science and Technology Project (Grant No. 18ZXJMTG00220), and the Fundamental Research Fund for the Central Universities of China. Reference 45 and a citation to Figure 1 was corrected on September 16, 2021 after initial online publication.

Conflict of Interest

The authors declare no conflict of interest.

Author Contributions

Q.Z. and D.R. contributed equally to this work. X.Z. supervised the project. Q.Z. designed and executed the experiments. D.R. conducted the operando Raman step and data processing. J. L., S.P., and M.W. aided in the course of the experiment. J.L. and X.Z. provided the experiment platform. J.L., M.G., and Y.Z. provided constructive advice. X.Z., M.G., Q.Z., and D.R. contributed to the writing of the manuscript. All authors discussed the results.

Data Availability Statement

Research data are not shared.

Keywords

CO₂ reduction, diffusion layer, increased concentration of CO₂, mass transport, micro-electrodes

Received: April 26, 2021

Revised: June 10, 2021

Published online: July 2, 2021

- [1] J. Durst, A. Rudnev, A. Dutta, Y. Fu, J. Herranz, V. Kaliginedi, A. Kuzume, A. A. Permyakova, Y. Paratcha, P. Broekmann, T. J. Schmidt, *Chimia* **2015**, *69*, 769.
- [2] S. J. Davis, K. Caldeira, H. D. Matthews, *Science* **2010**, *329*, 1330.
- [3] Y. Y. Birdja, E. Pérez-Gallent, M. C. Figueiredo, A. J. Göttle, F. Calle-Vallejo, M. T. M. Koper, *Nat. Energy* **2019**, *4*, 732.
- [4] N. S. Lewis, D. G. Nocera, *Proc. Natl. Acad. Sci. USA* **2006**, *103*, 15729.
- [5] J. H. Montoya, L. C. Seitz, P. Chakthranont, A. Vojvodic, T. F. Jaramillo, J. K. Nørskov, *Nat. Mater.* **2017**, *16*, 70.
- [6] D. U. Nielsen, X. M. Hu, K. Daasbjerg, T. Skrydstrup, *Nat. Catal.* **2018**, *1*, 244.

- [7] D. T. Whipple, P. J. A. Kenis, *J. Phys. Chem. Lett.* **2010**, *1*, 3451.
- [8] P. D. Luna, C. Hahn, D. Higgins, S. A. Jaffer, T. F. Jaramillo, E. H. Sargent, *Science* **2019**, *364*, eaav3506.
- [9] Z. Z. Wu, F. Y. Gao, M. R. Gao, *Energy Environ. Sci.* **2021**, *4*, 1121.
- [10] Hori, Y., *Mod. Aspects Electrochem.* **2012**, *42*, 89.
- [11] Y. Jiao, Y. Zheng, P. Chen, M. Jaroniec, S. Z. Qiao, *J. Am. Chem. Soc.* **2017**, *139*, 18093.
- [12] C. W. Li, M. W. Kanan, *J. Am. Chem. Soc.* **2012**, *134*, 7231.
- [13] M. Ma, K. Djanashvili, W. A. Smith, *Angew. Chem., Int. Ed.* **2016**, *55*, 6680.
- [14] A. Wagner, C. D. Sahm, E. Reisner, *Nat. Catal.* **2020**, *3*, 775.
- [15] X. Wang, A. Xu, F. Li, S. Hung, D. Nam, C. M. Gabardo, Z. Wang, Y. Xu, A. Ozden, A. S. Rasouli, A. H. Ip, D. Sinton, E. H. Sargent, *J. Am. Chem. Soc.* **2020**, *142*, 3525.
- [16] I. Grigioni, L. K. Sagar, Y. C. Li, G. Lee, Y. Yan, K. Bertens, R. K. Miao, X. Wang, J. Abed, D. Won, F. Arquer, A. H. Ip, D. Sinton, E. H. Sargent, *ACS Energy Lett.* **2021**, *6*, 79.
- [17] F. P. García de Arquer, C. Dinh, A. Ozden, J. Wicks, C. Mccallum, A. R. Kirmani, D. Nam, C. Gabardo, A. Seifitokaldani, X. Wang, Y. C. Li, F. Li, J. P. Edwards, L. J. Richter, S. J. Thorpe, D. Sinton, E. H. Sargent, *Science* **2020**, *367*, 661.
- [18] K. Jiang, R. B. Sandberg, A. J. Akey, X. Liu, D. C. Bell, J. K. Nørskov, K. Chan, H. Wang, *Nat. Catal.* **2018**, *1*, 111.
- [19] A. Loiudice, P. Lobaccaro, E. A. Kamali, T. Thao, B. H. Huang, J. W. Ager, R. Buonsanti, *Angew. Chem., Int. Ed.* **2016**, *55*, 5789.
- [20] L. Wang, S. Nitopi, A. B. Wong, J. L. Snider, A. C. Nielander, C. G. Morales-Guio, M. Orazov, D. C. Higgins, C. Hahn, T. F. Jaramillo, *Nat. Catal.* **2019**, *2*, 702.
- [21] N. Yoshihara, A. Sano, M. Noda, T. Kato, *Chem. Lett.* **2020**, *49*, 1121.
- [22] M. Liu, Y. Pang, B. Zhang, P. D. Luna, O. Voznyy, J. Xu, X. Zheng, C. T. Dinh, F. Fan, C. Cao, F. P. G. Arquer, T. S. Safaei, A. Mepham, A. Klinkova, E. Kumacheva, T. Filleter, D. Sinton, S. O. Kelley, E. H. Sargent, *Nature* **2016**, *537*, 382.
- [23] Y. Wang, P. Han, X. Lv, L. Zhang, G. Zheng, *Joule* **2018**, *2*, 2551.
- [24] Y. J. Sa, C. W. Lee, S. Y. Lee, J. Na, U. Lee, Y. J. Hwang, *Chem. Soc. Rev.* **2020**, *49*, 6632.
- [25] H. Wang, Y. Tzeng, Y. Ji, Y. Li, J. Li, X. Zheng, A. Yang, Y. Liu, Y. Gong, L. Cai, Y. Li, X. Zhang, W. Chen, B. Liu, H. Lu, N. A. Melosh, Z. Shen, K. Chan, T. Tan, S. Chu, Y. Cui, *Nat. Nanotechnol.* **2020**, *15*, 131.
- [26] Y. Zhou, F. Che, M. Liu, C. Zou, Z. Liang, P. Luna, H. Yuan, J. Li, Z. Wang, H. Xie, H. Li, P. Chen, E. Bladt, R. Quintero-Bermudez, T. Sham, S. Bals, J. Hofkens, D. Sinton, G. Chen, E. H. Sargent, *Nat. Chem.* **2019**, *11*, 1167.
- [27] J. Gao, H. Zhang, X. Guo, J. Luo, S. M. Zakeeruddin, D. Ren, M. Grätzel, *J. Am. Chem. Soc.* **2019**, *141*, 18704.
- [28] H. Xu, D. Rebolgar, H. He, L. Chong, Y. Liu, C. Liu, C. Sun, T. Li, J. V. Muntean, R. E. Winans, D. Liu, T. Xu, *Nat. Energy* **2020**, *5*, 623.
- [29] D. Ren, J. Gao, L. Pan, Z. Wang, J. Luo, S. M. Zakeeruddin, A. Hagfeldt, M. Grätzel, *Angew. Chem., Int. Ed.* **2019**, *58*, 15036.
- [30] D. Ren, J. Fong, B. S. Yeo, *Nat. Commun.* **2018**, *9*, 925.
- [31] Z. Xing, L. Hu, D. S. Ripatti, X. Hu, X. Feng, *Nat. Commun.* **2021**, *12*, 136.
- [32] R. M. Wightman, *Science* **1988**, *240*, 415.
- [33] R. M. Wightman, D. O. Wipf, *Electroanalytical Chemistry* (Ed.: A. J. Bard), Vol. 15, Marcel Dekker Inc., New York **1989**, p. 267.
- [34] M. Fleischmann, S. Pons, *Anal. Chem.* **1987**, *59*, 1391A.
- [35] M. Schreier, F. Héroguel, L. Steier, S. Ahmad, J. S. Luterbacher, M. T. Mayer, J. Luo, M. Grätzel, *Nat. Energy* **2017**, *2*, 17087.
- [36] S. Poulston, P. M. Parlett, P. Stone, M. Bowker, *Surf. Interface Anal.* **1996**, *24*, 811.
- [37] M. Deo, S. Mujawar, O. Game, A. Yengantiwar, A. Banpurkar, S. Kulkarni, J. Jog, S. Ogale, *Nanoscale* **2011**, *3*, 4706.
- [38] I. Oda, H. Ogasawara, M. Ito, *Langmuir* **1996**, *12*, 1094.
- [39] J. Shan, K. Katharina, P. Chiara, D. Holger, *J. Chem. Phys.* **2019**, *150*, 041718.
- [40] Y. Yang, S. Ajmal, Y. Feng, K. Li, X. Zheng, L. Zhang, *Chem. - Eur. J.* **2020**, *26*, 4080.
- [41] Y. Yang, L. Ohnouteck, S. Ajmal, X. Zheng, Y. Feng, K. Li, T. Wang, Y. Deng, Y. Liu, D. Xu, V. K. Valev, L. Zhang, *J. Mater. Chem. A* **2019**, *7*, 11836.
- [42] S. Ajmal, Y. Yang, M. A. Tahir, K. Li, A. Bacha, I. Nabi, Y. Liu, T. Wang, L. Zhang, *Catal. Sci. Technol.* **2020**, *10*, 4562.
- [43] W. Zhang, J. Ma, P. Wang, Z. Wang, F. Shi, H. Liu, *J. Membr. Sci.* **2016**, *502*, 37.
- [44] Y. Wang, C. Niu, Y. Zhu, D. He, W. Huang, *ACS Appl. Energy Mater.* **2020**, *3*, 9841.
- [45] Y. Wang, Y. Zhu, C. Niu, *J. Phys. Chem. Solids* **2020**, *144*, 109507.
- [46] C. C. L. McCrory, S. Jung, I. M. Ferrer, S. M. Chatman, J. C. Peters, T. F. Jaramillo, *J. Am. Chem. Soc.* **2015**, *137*, 4347.